Article

Numerical Simulation of Burst Failure in 2.5-Inch Unbonded Flexible Riser Pressure Armor Layers

Xiaoya Liu [1,†], Zhongyuan Qu [1,†], Yi Liu [1], Jiawei He [2], Guangju Si [1], Sicong Wang [1,*] and Qingsheng Liu [1,*]

1   School of Mechanical and Electric Engineering, Soochow University, Suzhou 215131, China; xyliu02100329@stu.suda.edu.cn (X.L.)
2   Naval Research Institute (NVRI), Beijing 100161, China
*   Correspondence: scwang8901@suda.edu.cn (S.W.); qsliu@suda.edu.cn (Q.L.); Tel.: +86-512-65790196 (Q.L.)
†   These authors contributed equally to this work.

Abstract: Unbonded flexible risers have been widely used in the field of offshore engineering in recent years due to their excellent performance in extreme dynamic marine environments, structural compliance, low installation cost, and low quality. And, the internal pressure capacity of unbonded flexible risers is an important indicator of the mechanical performance of unbonded flexible risers. Based on a 2.5-inch, 8-layer typical unbonded flexible riser model, this paper examines the burst failure of the pressure armor layer. Firstly, the balance equation of each separate cylindrical layer and helical layer is derived by functional principle, and then the overall theoretical modeling of an unbonded flexible riser under axisymmetric loads is established by additionally considering the geometric relation between adjacent layers. Secondly, fully considering the complex cross-sectional geometric characteristics and the interlayer's contact with the unbonded flexible riser, a simplified numerical 7-layer model is established by Abaqus, and the material with elastic-plastic properties is conferred. Finally, the validity of the proposed theoretical and numerical methods is verified through the axisymmetric behavior of the test data. Then the burst failure of the pressure armor layer is analyzed based on the material. At an internal pressure of 42 MPa, the pressure armor layer reached its yield stress of 300 MPa, with the entire cross-section yielding between 42 MPa and 42.5 MPa. Additionally, the effect of the friction coefficient is examined.

Keywords: unbonded flexible riser; internal pressure; bursting; pressure armor layer

1. Introduction

Unbonded flexible risers (see Figure 1) have become key equipment for deep-sea oil and gas resource development by virtue of their novel structural form, superior mechanical properties, and flexible arrangement of internal layer structure. Unbonded flexible risers consist of a composite of a helical steel metal armor layer with high stiffness and a polymer sealing layer with low stiffness. Each of the internal, separate layers has its own special function. As for the steel helical layers, the innermost carcass layer is a steel self-locking structure with an S-type geometric section, which is set to prevent the collapse of an unbonded flexible riser; the form of a pressure armor layer is similar to that of a carcass layer, which mainly provides the radial stiffness of an unbonded flexible riser; the tensile armor layer contains several helical tendons with a regular rectangular geometric section and typically has double or four layers that are relative winded, which is used for providing axial stiffness, bearing the role of axial tension and torque. Sometimes, also according to the riser by CO_2 and other media corrosion [1] and other actual conditions, some special functional layers can be flexibly designed according to the needs of the actual situation, such as the H_2S gas corrosion-resistant layer, thermal insulation layer, and anti-birdcage tape [2]. Also, a composite armor layer is developed for ultra-deep-sea oil and gas development [3,4].
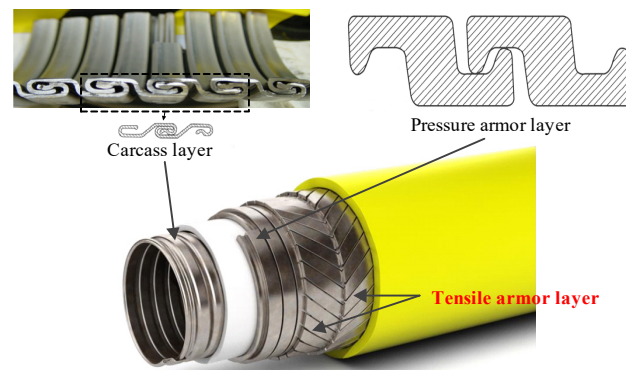
Figure 1. Sketch of a typical unbonded flexible riser.

The pressure armor layer [5,6] typically has different cross-sectional forms (see Figure 2), among which the Z-type is the most applied. The pressure armor layer is one of the important layers in an unbonded flexible riser, which mainly bears the internal pressures of the unbonded flexible riser. Unbonded flexible risers are subject to oversized internal pressure during operation, especially at the seabed where subsea oil and gas extraction locations are located. When the internal pressure inside the riser exceeds the internal pressure-bearing capacity of the riser, burst failure will occur, resulting in huge economic losses and environmental pollution [7–9]. Therefore, the prediction of bursting failure characteristics of pressure armor layers is of great significance.
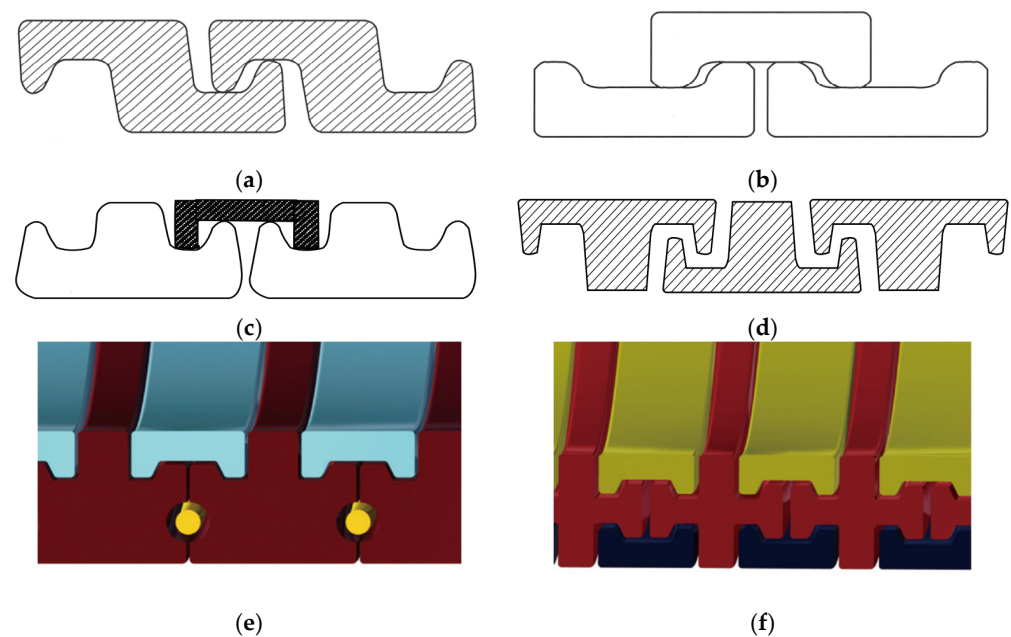
Figure 2. Profiles of the pressure armor layer (**a**) Z type; (**b**) C type; (**c**) T type–1; (**d**) T type–2; (**e**) K type; (**f**) X type. These subfigures represent different profiles of the pressure armor layer.

Analytical and numerical analysis of the cross-sectional properties of unbonded flexible risers is the common research method since test measurement is not only expensive and time-consuming, but also some special test equipment is sometimes needed and harsh conditions of the test are conducted. Compared with other mechanical cross-sectional properties of unbonded flexible risers [10,11], the burst failure characteristics of the pressure armor layer are relatively rare since the geometric properties of unbonded flexible risers are complex and most studies have simplified the pressure armor layer to a cylindrical layer. There are still some studies concentrated on this topic.

For test measurement, Kagoura et al. [12] applied internal pressure to a flexible pipe and observed the cross-section, which found that the pressure armor layer was the first to cause fracture failure, confirming that the pressure armor layer carries most of the internal pressure. Witz [13] investigated the effect of internal pressure on bending by giving the moment-curvature curves at an internal pressure of 30 MPa and found that the bending stiffness decreased after the application of internal pressure, but they did not add the internal pressure to the riser burst. Magluta et al. [14], Bech and Skallerud [15], Ma et al. [16], and Troina et al. [17] also studied the combined effect of internal pressure and bending moment by means of experimental methods, but they did not further study the burst failure of the pressure armor layer. Additionally, Ramos et al. [18]. gave experimental results for a 2.5-inch riser under a combination of axial and internal radial forces. Researchers mostly adopted theoretical and numerical methods, but they mainly concentrated on the axial tensile behavior of unbonded flexible risers [11,19,20].

Theoretical and numerical methods are the main analytical methods to study the cross-sectional behavior of an unbonded flexible riser. Theoretically, it is a more accurate algorithm to determine the burst pressure from a detailed stress analysis of the entire cross-section of the unbonded flexible riser [21–26]. Cylindrical shell-layer structures can be solved by considering the strains in the structure by means of the functional principle. While the helical layer can be divided into layers with regular cross-section (tensile armor layer) and with irregular cross-section (pressure armor layer and carcass layer), both considering the axial strain along the helical tendon, the tensile armor layer additionally considers the radial strain [27,28]. Numerically, existing studies of burst failure analysis of the pressure armor layer are relatively limited. Among them, Berge et al. [21] proposed a fast-calculating method for the overall response of an unbonded flexible riser and provided an expression for the stress-strain relationship under internal pressure alone; however, this theoretical method is not applicable to the calculation of multiple external loads and cannot decouple the response characteristics of each layer. Féret and Bournazel [22] present an analytical method to quickly assess the stress of the helical tendon while ignoring the effects of internal and external pressures and interlayer gaps in the unbonded flexible riser model, and it is concluded that the non-metallic cylindrical shell layer only transmits the interlayer pressures and ignores the role of its axial stiffness. Kebadze et al. [27,28] divided all interlayer structures of the unbonded flexible risers into cylindrical layers and helical layers, making a significant contribution to the response characteristics and mechanical analysis of the unbonded flexible riser under axisymmetric loads, but they also did not concentrate on the burst failure of the pressure armor layer. Neto et al. [29,30] proposed linear and nonlinear analytical equations for the analysis of burst failure of the pressure armor layer. They assumed that the pressure armor layer can be represented as a thin-walled cylinder and considered the thickness of the pressure armor layer equivalent to the Z-section, and reasonable results were obtained. Lanteigne [31] investigated the effect of internal radial pressure on the effective stiffness of helical armor layers. The carcass layer and pressure armor layer were simplified due to their self-locking caused by the unique helical single-wire-shaped cross-section of the carcass and tensile armor layers. Cuamatzi-Melendez [32] established a numerical model containing only the internal sheath layer and the pressure armor layer to study the internal pressure-carrying capacity of an unbonded flexible riser and compared it with the analytical method. They illustrated the importance of the numerical simulation and analysis method, but they did not take the effect of the tensile armor layer into account.

This paper aims to present the burst failure of the pressure armor layer and the pressure-bearing capacity of an unbonded flexible riser based on a numerical method. Based on a type of 2.5-inch unbonded flexible riser, a theoretical model of the riser under axisymmetric loads is established to calculate the axial and radial strains of the pressure armor layer. Additionally, a 7-layer simplified model neglecting the carcass layer is established by considering the force distribution characteristics and the material elasticity and plasticity of the pressure armor layer. The model was validated against existing test data,

showing a relative deviation of 6.32% for axial tensile behavior, confirming its accuracy. Based on the yield strength and ultimate strength of the material, the burst failure of the pressure armor layer is defined by the deformation from the numerical simulation, and the pressure-carrying capacity is investigated. In addition, the effect of the frictional coefficient was studied. This research contributes to a deeper understanding of unbonded flexible riser mechanical performance under internal pressure, providing valuable insights for offshore engineering applications.

2. Theoretical Formulations

The sketch of a loaded, unbonded flexible riser under axisymmetric loads is presented in Figure 3.
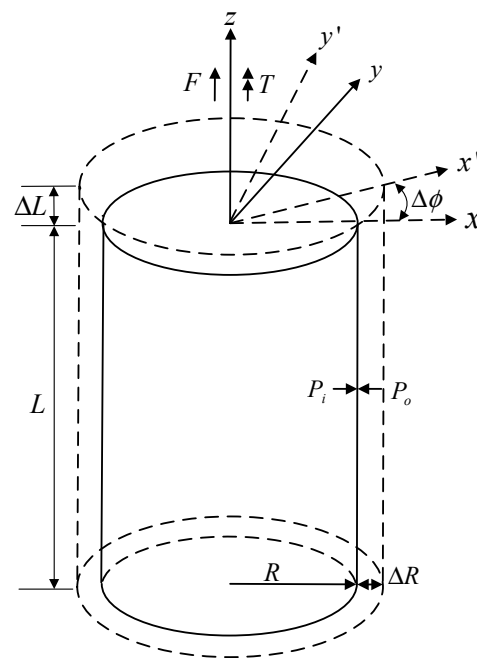
Figure 3. Sketch of an unbonded flexible riser under axisymmetric loads.

The theoretical model of the burst failure of the pressure armor layer must be built on some assumptions. The theoretical modeling includes all balance equations of interlayers and takes into account the geometric relationship between adjacent layers as well as the effect of material nonlinearities. The cylindrical layer in unbonded flexible risers is solved by applying thin-walled cylinder theory and considering radial strain deployment; the axial tensile and radial strains are applied for the tensile armor layer, while only the axial deformation along the pressure armor axial direction is considered. And, based on the following theoretical assumptions, the theoretical model of this article is obtained [33–35]:

1. The materials of each layer (except for the pressure armor layer) are homogeneous and vary within the linear elastic range;
2. Neglecting the frictional energy caused by relative sliding between layers;
3. Neglecting the influence of bending stiffener;
4. It is believed that the thickness of each layer varies uniformly along the length of the riser;
5. The strain on all layers is small enough to meet the geometric linearity condition;
6. Neglecting initial defects generated during the manufacturing process;
7. It is considered that when the pressure armor layer reaches its yield stress, it still has some internal pressure-bearing capacity until it reaches the ultimate stress.

2.1. The Equilibrium Equation of the Cylindrical Layer under Axisymmetric Loads

The cylindrical layer in the unbonded flexible riser is mainly used to isolate the fluid inside and outside the pipe, to reduce the friction between the adjacent layers, and to prevent the wear of the structural surface of the steel layer. Assuming that the axisymmetric loads include axial force F, torsion T, internal and external pressure P_i and P_o, the energy W performed by the axisymmetric loads can be expressed as follows:

$$W = F\Delta L + T\Delta\varphi + P_i\Delta V_i - P_o\Delta V_o \tag{1}$$

where $\Delta\varphi$ is the rotational angle seen in Figure 3, which is caused by torsion; ΔL stands for the axial deformation along the axial direction of the riser; ΔV_i and ΔV_o are the volumetric deformation and can be expressed as follows [2,3,32–34]:

$$\Delta V_i = \pi\left(R_i + \Delta R - \frac{\Delta t}{2}\right)^2(L + \Delta L) - \pi R_i^2 L \approx \pi R_i L(2R_m\varepsilon_2 - t\varepsilon_3 + R_i\varepsilon_1) \tag{2}$$

$$\Delta V_o = \pi\left(R_o + \Delta R + \frac{\Delta t}{2}\right)^2(L + \Delta L) - \pi R_o^2 L \approx \pi R_o L(2R_m\varepsilon_2 + t\varepsilon_3 + R_o\varepsilon_1) \tag{3}$$

where R_m, R_i, R_o are the average, internal, and external radii, separately; L is the riser's length; thickness and thickness deformation are defined by t and Δt; and the corresponding strains are defined by ε_1, ε_2, ε_3, as follows:

$$\begin{bmatrix} \varepsilon_1 \\ \varepsilon_2 \\ \varepsilon_3 \end{bmatrix} = \begin{bmatrix} \frac{\Delta L}{L} \\ \frac{\Delta R}{R_m} \\ \frac{\Delta t}{t} \end{bmatrix} \tag{4}$$

Thus, Equation (1) can be rewritten as follows:

$$W = (F\varepsilon_1 + T\gamma)L + \pi P_i R_i L(2R_m\varepsilon_2 - t\varepsilon_3 + R_i\varepsilon_1) - \pi P_o R_o L(2R_m\varepsilon_2 + t\varepsilon_3 + R_o\varepsilon_1) \tag{5}$$

where $\gamma = \Delta\varphi/L$.

Based on Hooke's law, the relationship between strain and stress based on Hooke's law can be given by the following:

$$\begin{aligned} \sigma_1 &= \frac{\mu E}{(1+\mu)(1-2\mu)}(\varepsilon_1 + \varepsilon_2 + \varepsilon_3) + \frac{E}{1+\mu}\varepsilon_1 \\ \sigma_2 &= \frac{\mu E}{(1+\mu)(1-2\mu)}(\varepsilon_1 + \varepsilon_2 + \varepsilon_3) + \frac{E}{1+\mu}\varepsilon_2 \\ \sigma_3 &= \frac{\mu E}{(1+\mu)(1-2\mu)}(\varepsilon_1 + \varepsilon_2 + \varepsilon_3) + \frac{E}{1+\mu}\varepsilon_3 \\ \tau &= \frac{E}{2(1+\mu)}\gamma \end{aligned} \tag{6}$$

where σ_1, σ_2, σ_3, and τ are the corresponding stresses of each direction, and E and μ are the material constants representing Young's modulus and Poisson's ratio, respectively.

The strain energy U can be represented by the following:

$$\begin{aligned} U &= \frac{1}{2}\int_V (\sigma_1\varepsilon_1 + \sigma_2\varepsilon_2 + \sigma_3\varepsilon_3 + \tau_{12}\gamma_{12})dV \\ &= \frac{1}{2}\int_V \left[(\lambda + 2G)(\varepsilon_1^2 + \varepsilon_2^2 + \varepsilon_3^2) + 2\lambda(\varepsilon_1\varepsilon_2 + \varepsilon_1\varepsilon_3 + \varepsilon_2\varepsilon_3) + GR_m^2\gamma^2\right]dV \end{aligned} \tag{7}$$

Then, based on principle of least potential energy:

$$\partial\Pi = \partial W - \partial U = 0 \tag{8}$$

Thus, according to Equations (5), (7), and (8), the equilibrium equations of the cylindrical layer under axisymmetric loads can be derived as follows:

$$
\begin{bmatrix} k_{11} & k_{12} & k_{13} & k_{14} \\ k_{21} & k_{22} & k_{23} & k_{24} \\ k_{31} & k_{32} & k_{33} & k_{34} \\ k_{41} & k_{42} & k_{43} & k_{44} \end{bmatrix} \begin{bmatrix} \Delta L/L \\ \Delta \phi/L \\ \Delta R/R_m \\ \Delta t/t \end{bmatrix} = \begin{bmatrix} F + \pi P_i R_i{}^2 - \pi P_o R_o{}^2 \\ T \\ 2\pi R_m (P_i R_i - P_o R_o) \\ -\pi t (P_i R_i + P_o R_o) \end{bmatrix} \tag{9}
$$

where

$$
\begin{aligned}
k_{11} &= \frac{\mu E A}{(1+\mu)(1-2\mu)} + \frac{EA}{1+\mu} & k_{13} = k_{31} &= \frac{\mu E A}{(1+\mu)(1-2\mu)} \\
k_{22} &= \frac{E}{2(1+\mu)} \cdot \frac{\pi}{2}\left(R_o{}^4 - R_i{}^4\right) & k_{24} = k_{42} &= 0 \\
k_{34} &= k_{43} = \frac{\mu E A}{(1+\mu)(1-2\mu)} & k_{12} = k_{21} &= 0 \\
k_{14} &= k_{41} = \frac{\mu E A}{(1+\mu)(1-2\mu)} & k_{23} = k_{32} &= 0 \\
k_{33} &= \frac{\mu E A}{(1+\mu)(1-2\mu)} + \frac{EA}{1+\mu} & k_{44} &= \frac{\mu E A}{(1+\mu)(1-2\mu)} + \frac{EA}{1+\mu}
\end{aligned}
$$

2.2. The Equilibrium Equation of the Helical Layer under Axisymmetric Loads

The sketch of a helical layer under external loads is present in Figure 4. Helical layers are the main structures that bear external loads of the unbonded flexible riser with a high laying angle.
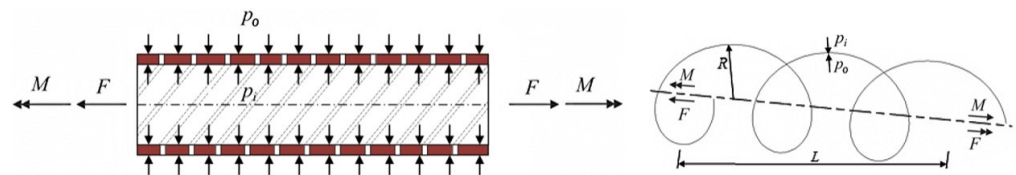
Figure 4. Sketch of the helical layer under external loads.

The axial strain ε_a of a helical layer (including the carcass layer, pressure armor layer, and tensile armor layer) can be defined by [22,27]:

$$
\varepsilon_a = \cos^2 \alpha \frac{\Delta L}{L} + R_m \sin \alpha \cos \alpha \frac{\Delta \varphi}{L} + \sin^2 \alpha \frac{\Delta R}{R_m} \tag{10}
$$

The radial deformation of the carcass and pressure armor layer with a complex cross section is difficult to define directly. While as for the tensile armor layer with regular geometric cross-section, the radial deformation ε_r is also considered and can be given by the following:

$$
\varepsilon_r = \frac{\Delta t}{t} \tag{11}
$$

Based on Equation (10), the strain energy U_s^1 of the carcass and pressure armor layer can be defined as follows [32–34]:

$$
U_s^1 = \frac{n}{2} \int_v \sigma \varepsilon_a dv \tag{12}
$$

where n is the number of helical tendons.

Based on Equations (10) and (11), the corresponding strain energy U_s^2 of tensile armor layer is given by the following [3,4]:

$$
U_s^2 = \frac{n}{2} \int_V (\sigma_a \varepsilon_a + \sigma_r \varepsilon_r) dV \tag{13}
$$

Also, based on the principle of least potential energy (Equation (8)), the balance equation for the carcass and pressure armor layer is obtained by the following [36–38]:

$$\begin{bmatrix} k_{11}^{ebt} & k_{12}^{ebt} & k_{13}^{ebt} \\ k_{21}^{ebt} & k_{22}^{ebt} & k_{23}^{ebt} \\ k_{31}^{ebt} & k_{32}^{ebt} & k_{33}^{ebt} \end{bmatrix} \begin{bmatrix} \Delta L/L \\ \Delta\phi/L \\ \Delta R/R_m \end{bmatrix} = \begin{bmatrix} F + \pi P_i R_i^2 - \pi P_o R_o^2 \\ T \\ 2\pi R_m(P_i R_i - P_o R_o) \end{bmatrix} \tag{14}$$

where
$$\begin{array}{ll} k_{11}^{ebt} = nEA\cos^3\alpha & k_{12}^{ebt} = k_{21}^{ebt} = nEAR_m\sin\alpha\cos^2\alpha \\ k_{13}^{ebt} = k_{31}^{ebt} = nEA\sin^2\alpha\cos\alpha & k_{22}^{ebt} = nEAR_m^2\sin^2\alpha\cos\alpha \\ k_{23}^{ebt} = k_{32}^{ebt} = nEAR_m\sin^3\alpha & k_{33}^{ebt} = nEA\frac{\sin^4\alpha}{\cos\alpha} \end{array}.$$

The balance equation for the tensile armor layer is obtained by the following [3,4]:

$$\begin{bmatrix} k_{11} & k_{12} & k_{13} & k_{14} \\ k_{21} & k_{22} & k_{23} & k_{24} \\ k_{31} & k_{32} & k_{33} & k_{34} \\ k_{41} & k_{42} & k_{43} & k_{44} \end{bmatrix} \begin{bmatrix} \Delta L/L \\ \Delta\phi/L \\ \Delta R/R_m \\ \Delta t/t \end{bmatrix} = \begin{bmatrix} F + \pi P_i R_i^2 - \pi P_0 R_0^2 \\ T \\ 2\pi R_m(P_i R_i - P_0 R_0) \\ -\pi t(P_i R_i + P_0 R_0) \end{bmatrix} \tag{15}$$

where

$$\begin{array}{ll} k_{11} = \frac{nEA}{1-\mu^2}\cos^3\alpha & k_{12} = \frac{nEAR_m}{1-\mu^2}\sin\alpha\cos^2\alpha \\ k_{13} = k_{31} = \frac{nEA}{1-\mu^2}\sin^2\alpha\cos\alpha & k_{14} = k_{41} = \frac{nEA\nu}{1-\mu^2}\cos\alpha \\ k_{22} = \frac{nEAR_m^2}{1-\mu^2}\sin^2\alpha\cos\alpha & k_{23} = k_{32} = \frac{nEAR_m}{1-\mu^2}\sin^3\alpha \\ k_{24} = k_{42} = \frac{nEAR_m\mu}{1-\mu^2}\sin\alpha & k_{33} = \frac{nEA}{1-\mu^2}\frac{\sin^4\alpha}{\cos\alpha} \\ k_{34} = k_{43} = \frac{nEA\mu}{1-\mu^2}\frac{\sin^2\alpha}{\cos\alpha} & k_{44} = \frac{nEA}{(1-\mu^2)\cos\alpha} \end{array}$$

When subjected to axisymmetric load, the helical tendon deforms only along its own axial direction, and the corresponding axial strain and the radial strain can be expressed by Equations (10) and (11). For the steel homogeneous isotropic material, only the axial stress of a pressure armor layer is considered and can be expressed as follows:

$$\sigma_a = E\varepsilon_a \tag{16}$$

2.3. Theoretical Model under Axisymmetric Loads

The interlayers of the unbonded flexible riser model are connected by the top ends, and under axisymmetric loading, it can be assumed that the axial elongation and torsional deformation of each layer are coordinately equal. Thus, the circumferential and radial formulas for each layer under internal and external pressures are as follows:

$$(k_{41})_j\frac{\Delta L}{L} + (k_{42})_j\frac{\Delta\varphi}{L} + (k_{43})_j\frac{(\Delta R)_j}{R_j} + (k_{44})_j\frac{(\Delta t)_j}{t_j} = -\pi(P_i)_j(R_i)t_j - \pi(P_0)_j(R_0)_j t_j \tag{17}$$

$$(k_{31})_j\frac{\Delta L}{L} + (k_{32})_j\frac{\Delta\varphi}{L} + (k_{33})_j\frac{(\Delta R)_j}{R_j} + (k_{34})_j\frac{(\Delta t)_j}{t_j} = 2\pi(P_i)_j(R_i)_j^2 - 2\pi(P_0)_j(R_0)_j^2 \tag{18}$$

Combined with the continuity boundary condition equations for the displacements between adjacent layers:

$$u_{R,j} - u_{R,j+1} + (u_{i,j} + u_{i,j+1})/2 = 0, (j = 1, 2, \ldots, N_t - 1) \tag{19}$$

where $u_{r,j}$ and $u_{t,j}$ are the mean radius and thickness variations in layer j, respectively.

Thus, the circumferential and radial strains and the contact pressures in each layer of the unbonded flexible riser under axisymmetric loading can be solved. When the neighboring layer starts to separate, i.e., there is a gap between neighboring layers, the contact pressure is set to 0. Based on the above equation, the analytical solution under axisymmetric loads can be obtained.

3. Numerical Simulation

3.1. Overall FE Model of Burst Failure Analysis of Unbonded Flexible Riser

Based on Witz's model [13], the finite element model of a typical 2.5-inch unbonded flexible riser is built by Abaqus software of 6.13 version, including detailed geometric properties of the pressure armor layer and two tensile armor layers with opposite winding angles, and a sketch of the geometric properties of the pressure armor layer is present in Figure 5 (unit: mm). The overall geometric and material characteristics of the unbonded flexible riser model are presented in Table 1, and a sketch of the numerical model is illustrated in Figure 6.
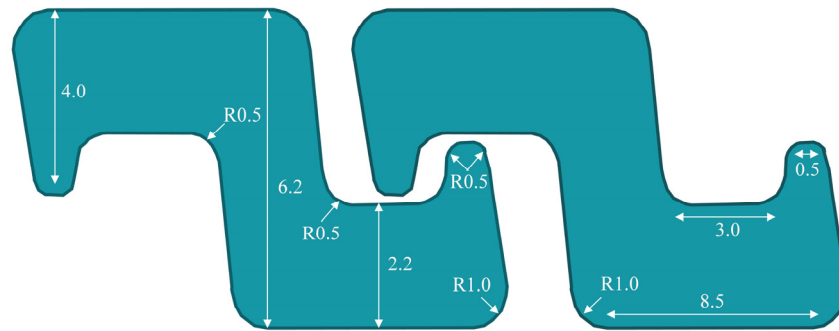
Figure 5. Cross-section of the pressure armor layer.

(**a**)

(**b**)
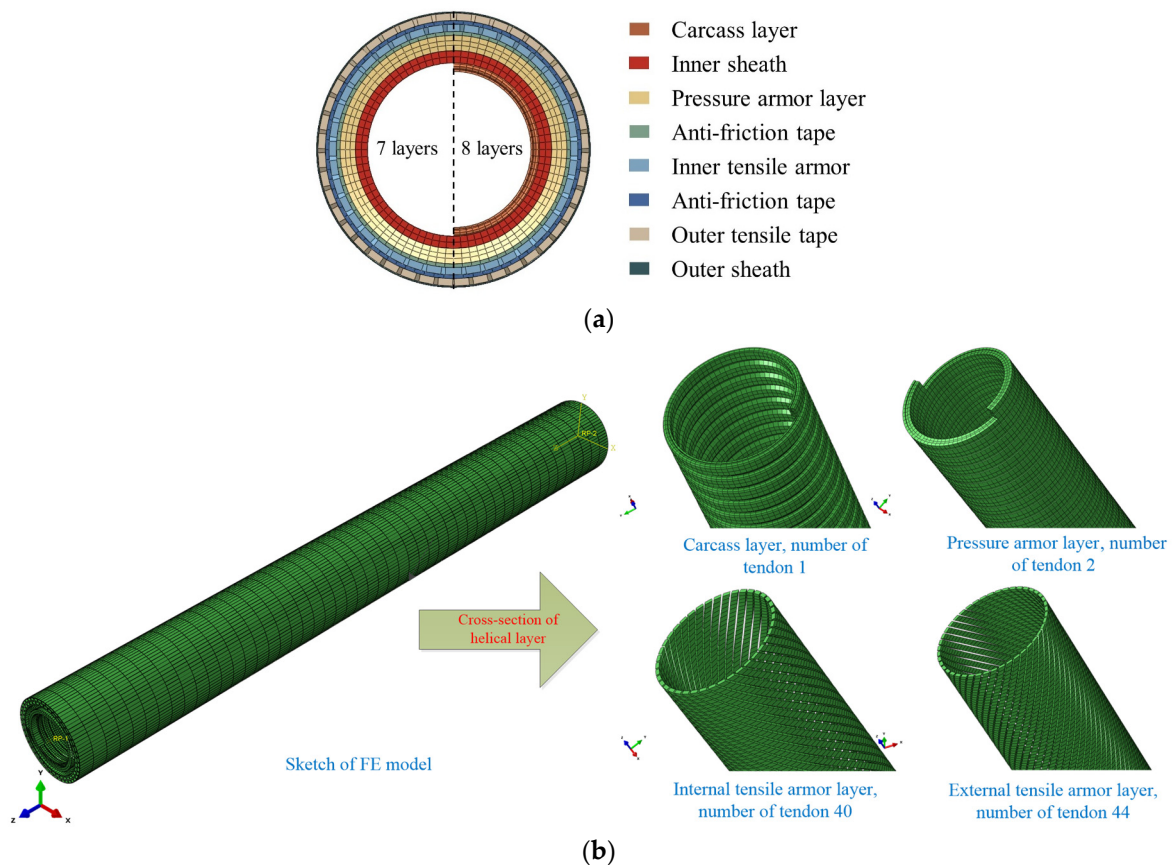
Figure 6. Finite element model of an unbonded flexible riser. (**a**) Cross-section of an unbonded flexible riser FE model; (**b**) Sketch of an 8-layer FE mode.

Table 1. Geometric and material properties of the unbonded flexible riser model.

Layer Number	Layer Type	Section Size (mm²)	Number of Tendons	Inner Radius (mm)	Outer Radius (mm)	Laying Angle (°)	Material	Young's Modulus (GPa)	Poisson's Ratio
1	Carcass	19.60	1	31.60	35.10	−87.5	AISI 304	205	0.29
2	Pressure sheath	-	-	35.10	40.00	-	Nylon 12	0.28	0.30
3	Zeta layer	5.55	1	40.05	46.25	−85.5	FI-15	205	0.29
4	Anti-friction layer	-	-	46.25	47.75	-	Nylon 11	0.30	0.30
5	Inner tensile armor layer	18.00	40	47.75	50.75	−35.0	FI-41	205	0.29
6	Anti-friction layer	-	-	50.75	52.25	-	Nylon 11	0.30	0.30
7	Outer tensile armor layer	18.00	44	52.25	55.25	35.0	FI-41	205	0.29
8	Fabric tape	4.50	-	55.25	55.75	-	-	0.60	0.30

Some settings related to numerical modeling are presented first. The numerical model of unbonded flexible risers needs to have sufficient length to reduce the influence of end effects [39], thus the model is taken as 1 m, about twice the tensile armor layer's pitches in this paper. Due to the fact that the innermost carcass layer is a non-watertight structure, it usually does not provide internal pressure-bearing capacity, where oil and gas would directly act on the internal sheath. Therefore, a numerical model without a carcass layer is simplified to a 7-layer model for numerical simulation (see Figure 6a). For comparison reasons, the behavior of an 8-layer model is also present, and in the following analysis, it is found that the relative error between the full-layer model and the simplified model is small enough that the simplification is reasonable when an unbonded flexible riser model is under internal pressure. The overall finite element model of the unbonded flexible pipe is shown in Figure 6b.

In order to accurately obtain the detailed deformation of each layer and the stress distribution along the riser model, the uncompliant 8-node linear hexahedral element (C3D8I element in ABAQUS) was used to simulate all the interlayers of an unbonded flexible riser.

3.2. Boundary Condition

In order to facilitate the control of the boundary conditions and apply external loads to the numerical model, two reference points (top RP-1 and bottom RP-2, see Figure 7) were set at the center of the cross-section at both ends of the numerical model. This is because if the reference point is selected on the mesh at the edge of the end face, bending moments may be generated during loading, resulting in inaccurate results. All degrees of freedom of each interlayer at the end cross-section were kinematically coupled with the two reference points.

Among them, all degrees of freedom on the bottom RP-2 are constrained, and in addition, the twisting direction of the top RP-1 along the Z-axis (riser axis) is constrained. The internal pressure load of the model is achieved by applying uniformly distributed radial pressure to the inner surface of the pressure sheath.

Due to the possible gaps between the interlayers of unbonded flexible risers, there might be contact and sliding between layers during the application of loads, and the pressure armor layer might also experience self-contact within the layer, resulting in complex contact situations. Therefore, the general contact algorithm of Abaqus is adopted to model the contact simulation. In addition, the Coulomb friction model is adopted to

simulate the tangential behavior with a friction coefficient of 0.1 [40], while the normal contact is set to hard contact.
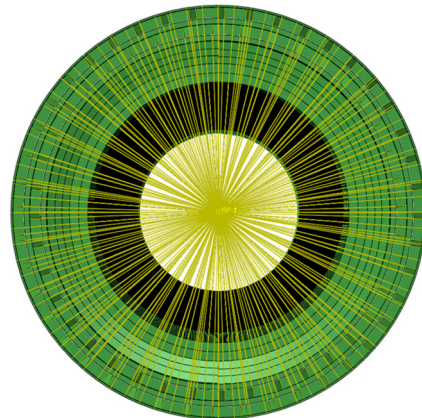
Figure 7. Kinematic coupling of the end points of an unbonded flexible riser on reference point RP-2.

3.3. Failure Determination

The yield strength of the pressure armor layer is defined by 300 MPa, and the corresponding ultimate strength is defined by 600 MPa [32]. A sufficiently large internal pressure is applied for the unbonded riser model to ensure the burst failure of the pressure armor layer. The internal pressure-axial tensile deformation curve, stress contour, and strain contour of the pressure armor layer are adopted to define the burst failure of the pressure armor layer. When the stress of the pressure armor is in the linear stage, the stress variation is relatively uniformly distributed. When the stress of the pressure armor layer enters the plasticity phase, the pressure armor layer is considered to remain compressive, despite being much reduced, until the element reaches ultimate stress and undergoes large deformation.

3.4. Load Loading and Time Step Control

Due to the complex structure of the model and the presence of a large number of contact problems, using the implicit solution method would bring significant convergence problems. Therefore, explicit solution methods are used for numerical computation. Although the explicit solution method can effectively solve the convergence problem in Abaqus, the inertia effect will seriously affect the numerical accuracy, and the kinetic energy during the simulation must be controlled. It is generally believed that the ratio of kinetic energy (ALLKE) to internal energy (ALLIE) should not exceed 5–10% during the whole numerical simulation process. The quasi-static loading method of increasing the loading time can be used to eliminate the influence of the inertia effect. However, too much loading time will reduce the computational efficiency. In this study, the loading time is chosen to be 0.3 s while satisfying the computational accuracy.

4. Model Verification

Since there is no relevant test data of unbonded flexible risers under internal pressure for comparison, the behavior of unbonded flexible risers under tension, which is also an axisymmetric load, is present first to verify the present theoretical and numerical methods. And then the behavior of an unbonded flexible riser under internal pressure is present.

Based on Witz's test, the tensile behavior of an unbonded flexible riser is exhibited in Figure 8. Unlike the test results, both the theoretical and numerical methods show near-linear change since the tensile armor layers do not have obvious slippage. The relative deviation between numerical and theoretical results is about 6.32%, which shows good agreement. And the deviation is mainly caused by the assumptions made in the theoretical method, for example, the uniformly distributed stress along the riser model. Meanwhile, the numerical method can properly predict the axial tensile stiffness of an unbonded flexile

riser compared to the test result, and the relative deviation is about 8.07%. Additionally, the average axial tensile stiffness predicted by other scholars and organizations is also present in Figure 8, and the proposed theoretical method in this paper has a better prediction.
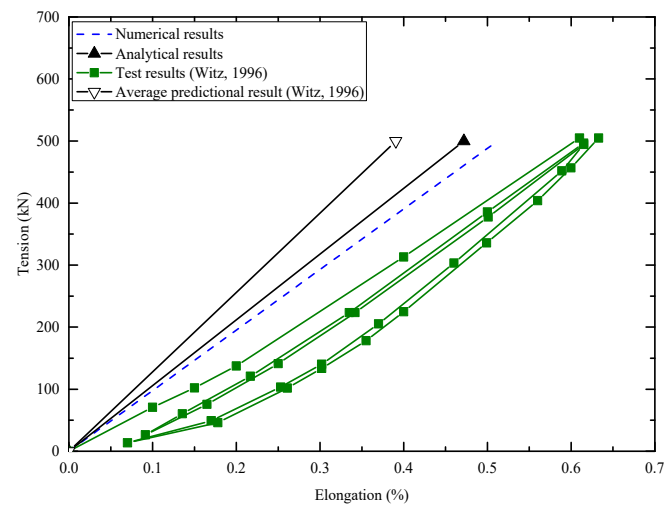
Figure 8. Axial tension-elongation curves of different methods [13].

The pressure expansion coefficient (ratio of internal pressure and axial elongation) is a significant indicator to study the effect of internal pressure [28]. Witz [13] did not give the experimental data under the action of internal pressure, so Figure 9 illustrates the comparison between the theoretical and numerical results in the linear phase of pressure armor layer material based on the above unbonded flexible riser model. From Figure 9, the two methods coincide well with each other, proving that the proposed numerical and theoretical methods can well predict the behavior of an unbonded flexible riser under internal pressure.
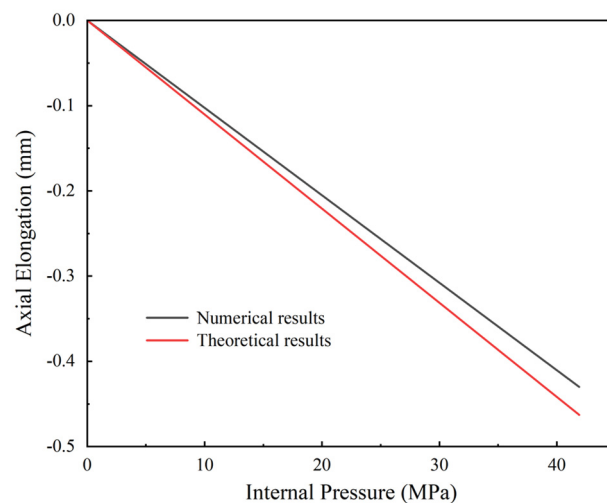
Figure 9. Relationship between internal pressure and axial displacement.

5. Results and Discussion

Since the innermost carcass layer is not a watertight structure and there is usually a gap with the internal sheath layer, a simplified unbonded flexible riser numerical model without carcass layer is proposed in this section to accelerate the calculation simulation and is also compared with the original 8-layer unbonded flexible riser model. Considering the elasticity of the pressure armor layer, burst failure is defined by the stress distribution and deformation from numerical simulation and the yield stress and ultimate stress from

theoretical calculation. In addition, the effect of the friction coefficient on the internal pressure-bearing capacity of an unbonded flexible riser is also discussed.

5.1. Burst Failure of the Pressure Armor Layer

First of all, the proposed numerical method presents a comparison between the full-layer unbonded flexible riser model and the simplified numerical model. Figure 10 presents the axial displacement-internal pressure relationship. And it can be seen from Figure 10 that, before the yield of the pressure armor layer, the numerical results from both models are close to linear and highly consistent. It is because the internal pressure was applied to the inner sheath layer, and the deformation of the carcass layer has little effect on the overall behavior of the unbonded flexible riser under internal pressure, verifying the effectiveness of the 7-layer simplified numerical model. As the internal pressure continuously increases and, by neglecting the nonlinear instability during numerical simulation, the pressure armor layer reaches yield stress, plastic deformation of the pressure armor layer occurs, and the pressure expansion coefficient decreases significantly. When the internal pressure exceeds about 62.4 MPa, there is a certain deviation between the two numerical models, which is mainly caused by the self-locking of the pressure armor layer, and the deformation of the pressure armor layer affects the deformation of the carcass layer, contributing to the difference. After the pressure armor layer reaches its ultimate strength, large plastic deformation with the increase in internal pressure load will occur, and the unbonded flexible riser model will lose its ability to stand internal pressure.
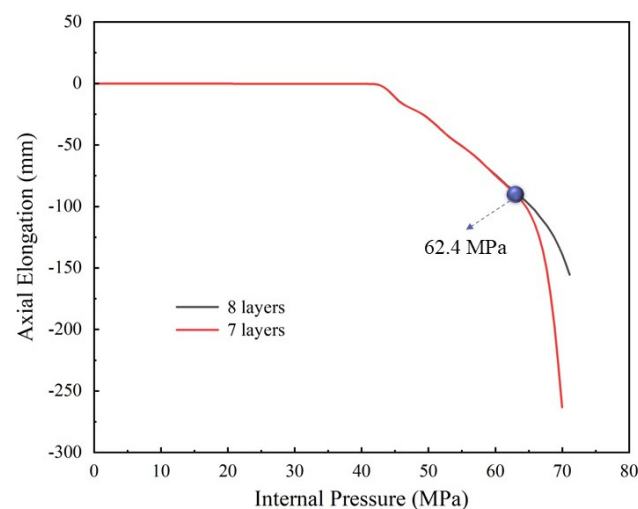
Figure 10. Comparison of internal pressure-axial elongation curves by full-layer model and simplified numerical model.

The ratio of ALLKE to ALLIE during the numerical calculation process is shown in Figure 11, and the maximum ratio is about 6%, indicating the correctness of the numerical method. It can be seen from Figure 11 that when the internal pressure exceeds about 60 MPa, the ratio has a gradually increasing growth rate, which is caused by the dynamic response of the increasing plastic deformation. It is also worth noting that this is consistent with the internal pressure values when the two models in Figure 10 begin to deviate.

Also, a theoretical prediction is compared with the numerical method based on the 8-layer riser model (see Figure 12), which shows good agreement. Since the application of the internal pressure load during the calculation of the theoretical results is directly applied to the internal sheath layer rather than on the carcass layer, and the deformation in the theoretical calculations does not lead to contact between the skeleton layer and the internal sheath layer, the theoretical results of the 7 and 8 layers are the same. In order to avoid repetition of the burdensome, we do not repeat the theoretical curve diagrams of the 7 layers in this paper. From the figure, we can see that the theoretical and numerical curves

converge before the yield strength is reached (i.e., the linear phase). Then the curves trend differently after failure due to the bending deformation of the numerical model with large deflections, which cannot be simulated by the current theoretical method.
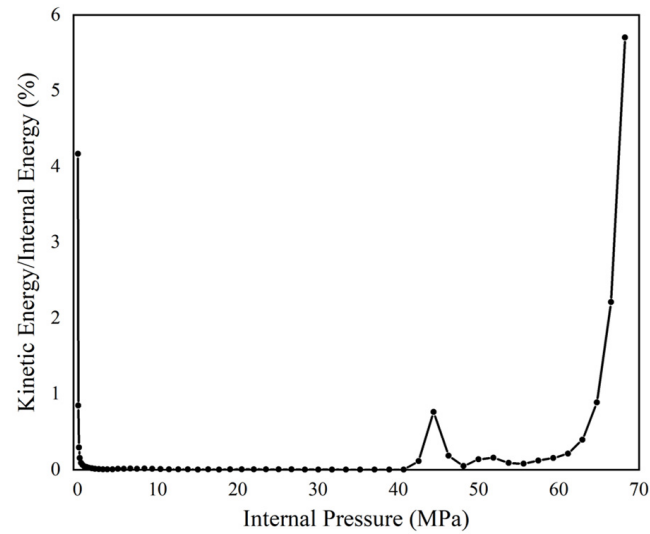
Figure 11. Ratio of ALLKE to ALLIE during numerical simulation.
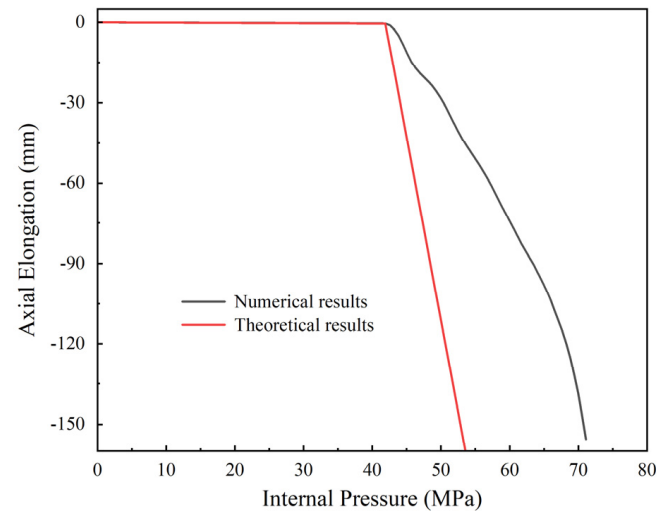
Figure 12. Internal pressure-axial elongation curve of the numerical method and the theoretical method.

The pressure armor layer is the main structure to withstand the internal pressure of unbonded flexible risers. In order to conduct a detailed study, the internal pressure-bearing capacity of the unbonded flexible riser and the stress and strain contours of the pressure armor are examined. By neglecting the stress concentration of the end boundary effect, the stress is relatively consistent and uniformly distributed during the internal pressure loading process. Therefore, a Z-shaped section near the middle part of the pressure armor layer is selected, and the stress contours under different internal pressures are present in Figure 13. To make it clear, the stress change range in the contour is fixed at 300 MPa; red markings are also used when the value is higher.

It can be seen from Figure 13 that the stress of the Z-shaped section gradually decreases from bottom to top (from the inner surface to the outer surface of the pressure armor layer), following the general law of stress variation along the thickness direction of the cross section under internal pressure. However, considering the particular geometry of the Z-shaped pressure armor layer, the maximum stress occurs at the sharp left and right ends. As the

internal pressure increases, the stress of the pressure armor layer increases continuously, and the innermost part of the section reaches yield first, then gradually expands to the outer part. When the internal pressure loading is between 42 MPa and 42.5 MPa, the entire section reaches yield stress, which is consistent with the range of the energy analysis above (see Figure 11).
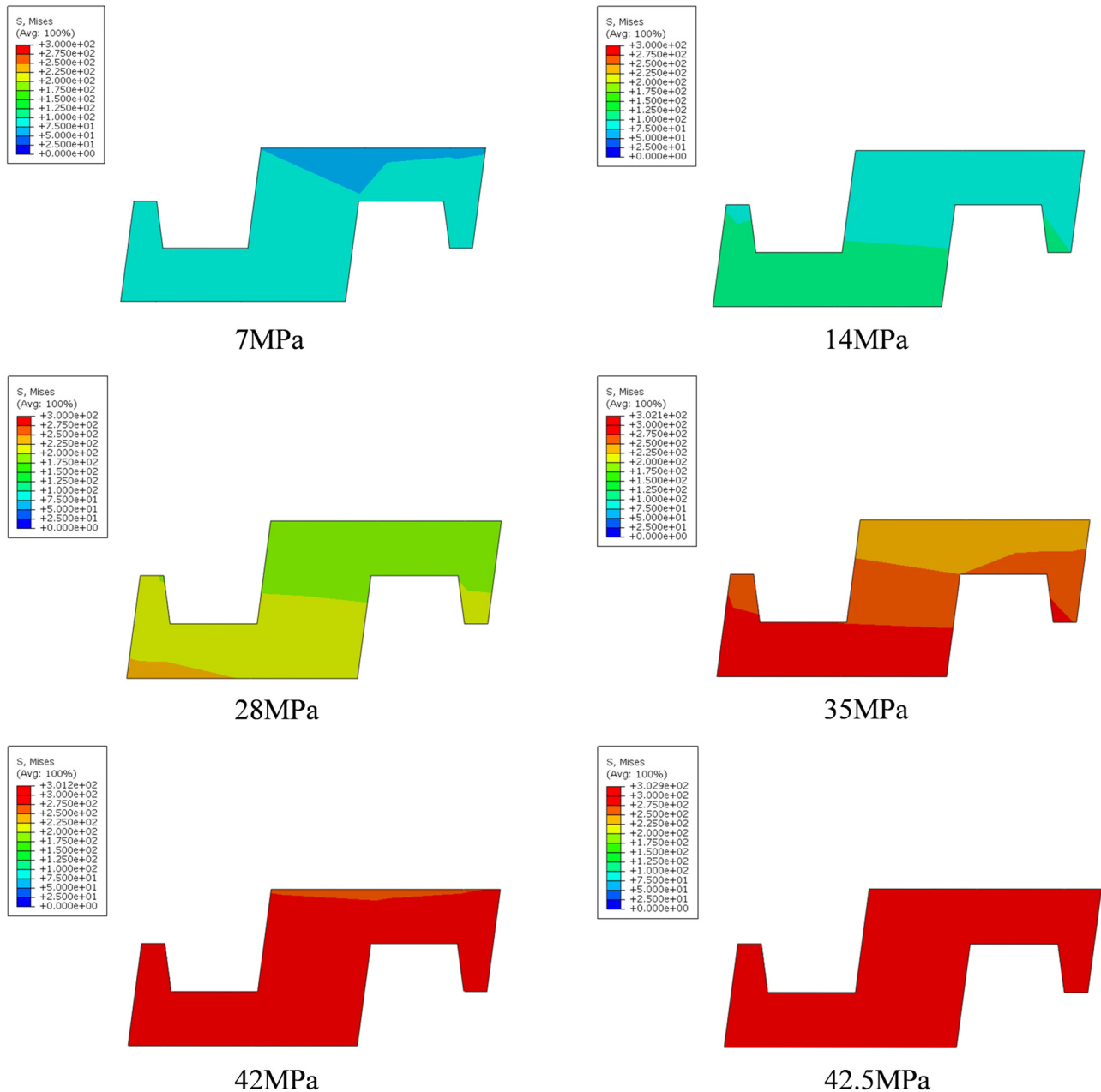
Figure 13. Stress contours of the pressure armor layer with a Z-shaped cross-section.

Judged by the yield stress of the pressure armor layer, the overall stress contours of the pressure armor layer are present in Figure 14. Figure 14a illustrates the stress contour of the pressure armor layer when it is about to reach the yield stress. Due to the influence of the end boundary effect, the stress distribution at both ends is significantly different from that in the middle of the layer. Meanwhile, it can be seen that the stress on the inner surface is significantly greater than that on the outer surface. The intersurface is directed to the inner sheath, where the internal pressure is loaded, and it bears more internal pressure than the outer part of the layer, which is consistent with Figure 13. Figure 8 exhibits the

stress contours of the pressure armor layer after 300 MPa. Due to the self-locking structure and hardening effect of the pressure armor layer, after the layer has basically reached yield stress, the axial stress deformation of the pipeline is still relatively consistent, and there is no stress concentration or local large deformation.

(**a**)

(**b**)
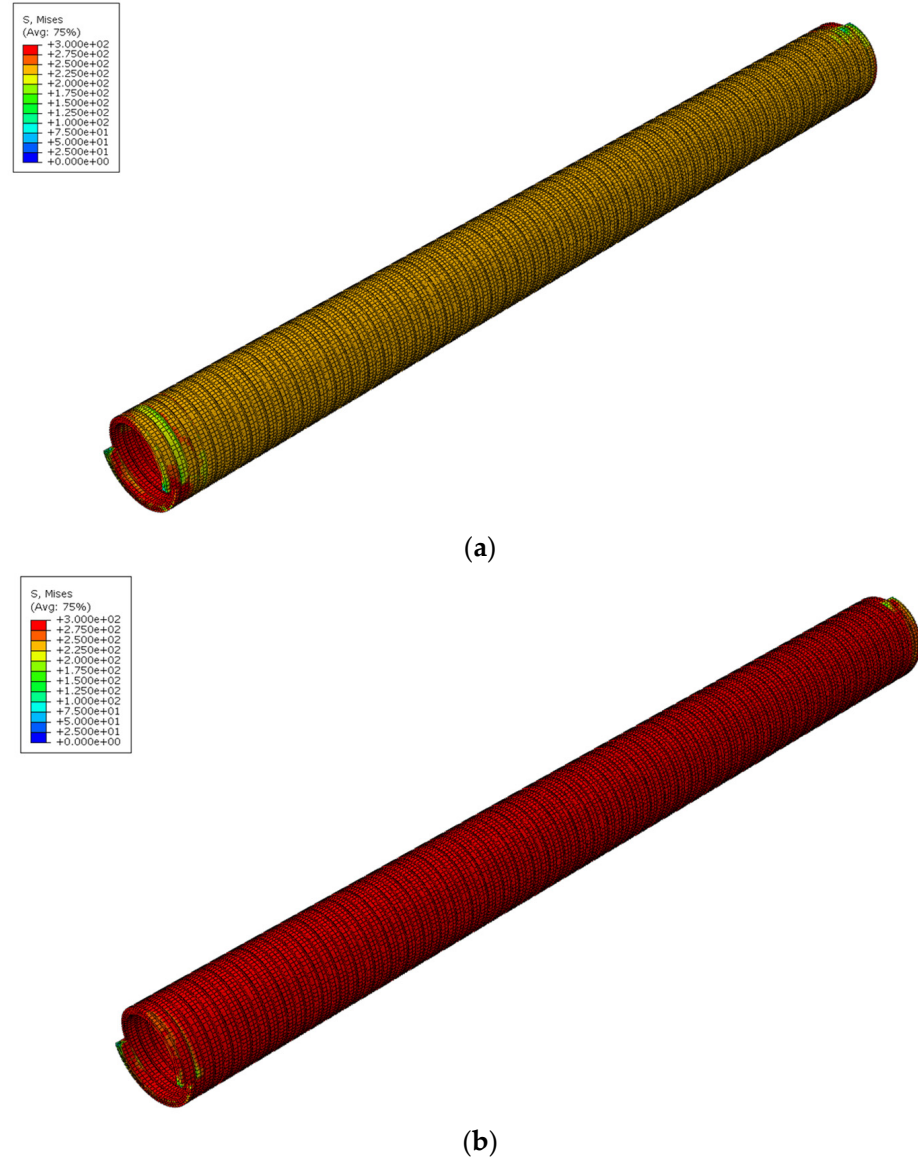
Figure 14. Stress contours of the pressure armor layer before and after 300 MPa: (**a**) stress contour before 300 MPa; (**b**) stress contour after 300 MPa.

As the internal pressure increases, the pressure armor layer near the top end first reaches the ultimate stress of 600 MPa, as shown in Figure 15. Under the action of internal pressure loading, significant irreversible plastic deformation occurs at both ends of the pressure armor layer, and the self-locking structure cracks and fails.
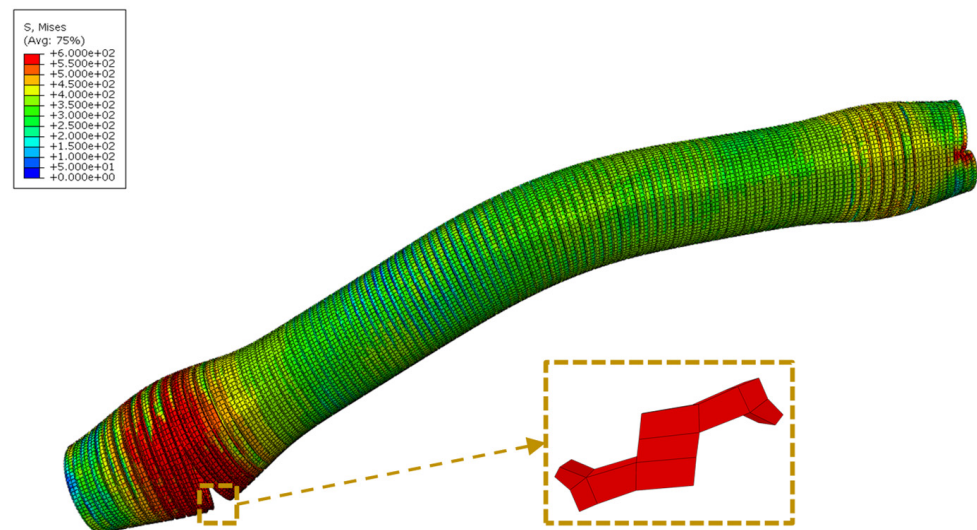
Figure 15. Stress contours of the pressure armor layer at 600 MPa.

5.2. Effect of Friction Coefficient

The unbonded flexible riser is exposed to the marine wet environment, which would affect the friction coefficient between and within the unbonded flexible riser model. Unbonded flexible risers experience axial displacement under internal pressure, and there would be a certain relative slippage resulting in a certain amount of friction energy, which thus might affect the burst failure characteristics of the pressure armor layer. As the theoretical method cannot include the effect of the friction coefficient, the proposed numerical method is applied to study the influence. And six loading cases with an interval of 0.02 of the friction coefficient from 0–0.1 are present.

Figure 16 shows the internal pressure-axial displacement relationship curve with different friction coefficients. The black solid line and the red solid line stand for the friction coefficients of 0 and 0.02, separately, which is significantly less than the ultimate internal pressure loading performance with friction coefficients from 0.04 to 0.1. When the friction coefficient is no more than 0.04, the mutual constraints between interlayers continue to increase, and the bearing capacity of the pressure armor layer is significantly improved, causing the burst failure of internal pressure to increase from 35.3 MPa to 55.8 MPa. When the friction coefficient is 0, the friction between adjacent layers and within helical layers is completely ignored, and the pressure armor layer loses the mutual constraint between layers, allowing for free sliding between layers. When the friction coefficient is over 0.04, the sensitivity of the internal pressure bearing capacity to the friction coefficient decreases while still showing an increasing trend, which indicates that there is no relative slippage between adjacent surfaces and that the friction coefficient has little effect on the critical burst failure. In conclusion, the internal sheath should avoid damage, thus ensuring the friction coefficient of the pressure armor layer and increasing the internal pressure-bearing capacity of the unbonded flexible riser.
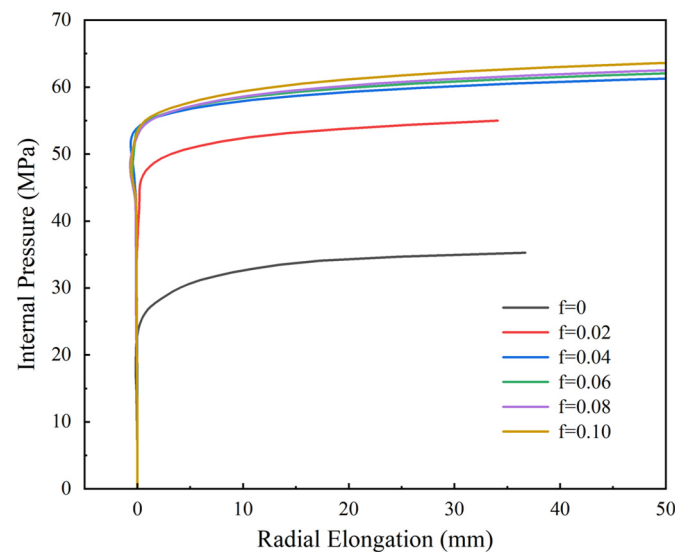
Figure 16. Internal pressure-radial displacement curve of a pressure armor layer with different friction coefficients.

6. Conclusions

This article explores the mechanical properties of a type of 2.5-inch unbonded flexible riser under internal pressure using a numerical method and verified through an analytical method. First of all, the theoretical model is established considering the material nonlinearity of the pressure armor layer. Afterwords, a simplified 7-layer model without carcass layer is established by considering the detailed geometric properties of interlayers within the Abaqus software, and the validity of the simplified model is verified through the full-layer numerical model and the proposed theoretical method. Finally, based on the yield and ultimate stress of the pressure armor layer, the burst failure process of the pressure armor layer is investigated. In addition, the influence of the friction coefficient on the burst failure of the pressure armor layer is also analyzed. Some conclusions are drawn at the end of this paper:

1. The internal pressure of unbonded flexible risers is mainly borne by the pressure armor layer, and the non-watertight structure of the carcass layer has little effect on the numerical modeling of the unbonded flexible riser with respect to the burst failure analysis of the pressure armor layer.

2. As the internal pressure loads, the stress distributes uniformly along the pressure armor layer, neglecting the end boundary effect. As for the Z-shaped section of the pressure armor layer, the stress gradually decreases from the inner layer to the outer layer, and the two sharp ends of the Z-shaped section first reach yield stress.

3. When the pressure armor layer is about to reach the yield stress, the stress distribution at both ends of the riser is significantly different from that in the middle section, and there is no stress concentration or local large deformation. When the stress exceeds the ultimate stress, significant plastic deformation occurs at the end of the pressure armor layer model, contributing to the burst failure.

4. The increasing friction coefficient can achieve the effect of increasing the internal pressure load capacity borne by the riser, which is related to interlayer slippage. The pressure armor layer should have a sufficient friction coefficient to ensure the internal pressure-bearing capacity of the pressure armor layer.

References

1. Lei, Q.; Hou, Z.; Zhu, X.; Chen, C. Study on torsional response and ultimate loading of unbonded flexible risers under corrosion defects. *Ocean Eng.* **2024**, *291*, 116413. [CrossRef]
2. Epsztein, T.; Demanze, F.; Lefebvre, X.; Jarrin, J. New anti H_2S layer for flexible pipes. In Proceedings of the Offshore Technology Conference, Houston, TX, USA, 2–5 May 2011; OTC 21371.
3. Lambert, A.; Do, A.; Felix-Henry, A.; Grosjean, F. Qualification of unbonded dynamic riser with carbon fiber composite armors. In Proceedings of the International Conference on Offshore Mechanics and Arctic Engineering, Rio de Janeiro, Brazil, 1–6 July 2012; pp. 117–125.
4. Liu, Q.; Xue, H.; Tang, W. Behavior of unbonded flexible riser with composite armor layers under coupling loads. *Ocean Eng.* **2021**, *239*, 109907. [CrossRef]
5. Fernando, U.; Dodds, N.; Graham, G.; Davidson, M.; Kirton, P.; Nott, P.; Thompson, A. Flexible Pipe Body and Method of Producing Same. U.S. Patent Application No. 15/147,802, 22 May 2017.
6. Rytter, J.; Rytter, N.; Nielsen, R.; Glejbøl, K. A novel compression armor concept for unbonded flexible pipes. In Proceedings of the Offshore Technology Conference, Houston, TX, USA, 6–9 May 2002. OTC-14059-MS.
7. Zhu, Z.; Song, Y.; Zhang, Y.; Liu, Q.; Wang, G. Sound radiation of the plate with arbitrary holes. *Int. J. Mech. Sci.* **2024**, *264*, 108814. [CrossRef]
8. Zhang, Y.; Zhu, Z.; Sheng, Z.; He, Y.; Wang, G. Sound absorption properties of the metamaterial curved microperforated panel. *Int. J. Mech. Sci.* **2024**, *268*, 109003. [CrossRef]
9. Zhu, Z.; Wang, G.; Sheng, Z.; Zhang, Y.; Xu, R. Sound insulation properties of embedded co-cured composite damping sandwich panel under arbitrary boundary conditions. *Mech. Syst. Signal Process.* **2023**, *204*, 110810. [CrossRef]
10. Wang, L.; Ye, N.; Yue, Q. A novel helix contact model for predicting hysteretic behavior of unbonded flexible pipes. *Ocean Eng.* **2022**, *264*, 112407. [CrossRef]
11. Liu, H.; Li, M.; Shen, Y. Numerical Analysis of Mechanical Behaviors of Composite Tensile Armored Flexible Risers in Deep-Sea Oil and Gas. *J. Mar. Sci. Eng.* **2023**, *11*, 619. [CrossRef]
12. Kagoura, T.; Ishii, K.; Abe, S.; Inoue, T.; Yamada, T. Development of a flexible pipe for pipe-in-pipe technology. *Furukawa Rev.* **2003**, *24*, 69–75.
13. Witz, J. A case study in the cross-section analysis of flexible risers. *Mar. Struct.* **1996**, *9*, 885–904. [CrossRef]
14. Magluta, C.; Roitman, N.; Viero, P.; Rosa, L.; Ribeiro, E. Experimental estimation of physical properties of a flexible riser. In Proceedings of the International Conference on Offshore Mechanics and Arctic Engineering, Rio de Janeiro, Brazil, 3–8 June 2001; pp. 255–264.
15. Bech, A.; Skallerud, B. Structural Damping in flexible pipes: Comparisons between dynamic tests and numerical simulations. In Proceedings of the International Offshore and Polar Engineering Conference, San Francisco, CA, USA, 14–19 June 1992; ISOPE-I-92-125.
16. Ma, W.; Su, L.; Wang, S.; Yang, Y.; Huang, W. Influence of structural parameters of unbonded flexible pipes on bending performance. *Ocean Eng.* **2022**, *266*, 113109. [CrossRef]
17. Troina, L.; Rosa, L.; Viero, P.; Magluta, C.; Roitman, N. An experimental investigation on the bending behaviour of flexible pipes. In Proceedings of the International Conference on Offshore Mechanics and Arctic Engineering, Cancun, Mexico, 8–13 June 2003. OMAE2003-37200.
18. Ramos, J.; Arruda, M.; Pesce, C.; Roveri, E. A case study on the axial-torsional behavior of flexible risers. In Proceedings of the International Conference on Offshore Mechanics and Arctic Engineering, Estoril, Portugal, 15–20 June 2008; pp. 481–491.
19. Lei, L.; Chen, C.; Zhu, X. Tensile failure behavior of unbonded flexible riser with damaged tensile armor wires. *Ocean Eng.* **2023**, *267*, 113112. [CrossRef]
20. Liu, W.; Wang, S. A Stiffness Surface Method to Analyze the Cross-Sectional Mechanical Properties of Reinforced Thermoplastic Pipes Subjected to Axisymmetric Loads. *J. Ocean. Univ. China* **2021**, *20*, 811–822. [CrossRef]

21. Berge, S.; Leira, B.; Nygaard, I.; Fylling, I.; Larsen, C.M.; Leira, B.J.; Nygaard, I.; Olufsen, A. *Handbook on Design and Operation of Flexible Pipes*; SINTEF: Oslo, Norway, 1992.

22. Féret, J.; Bournazel, C. Calculation of stresses and slip in structural layers of unbonded flexible pipes. *J. Offshore Mech. Arct. Eng.* **1987**, *109*, 263–269. [CrossRef]

23. Goto, Y.; Okamoto, T.; Araki, M.; Fuku, T. Analytical study of the mechanical strength of flexible pipes. *Brain Dev.* **1987**, *109*, 249–253. [CrossRef]

24. Noii, N.; Khodadadian, A.; Ulloa, J.; Aldakheel, F.; Wick, T.; François, S.; Wriggers, P. Bayesian inversion for unified ductile phase-field fracture. *Comput. Mech.* **2021**, *68*, 943–980. [CrossRef]

25. Mcnamara, J.; Harte, A. Three-Dimensional analytical simulation of flexible pipe wall structure. *J. Offshore Mech. Arct. Eng.* **1992**, *114*, 69–75. [CrossRef]

26. Harte, A.; Mcnamara, J. Modeling procedures for the stress analysis of flexible pipe cross sections. *J. Offshore Mech. Arct. Eng.* **1993**, *115*, 46–51. [CrossRef]

27. Kebadze, E. Theoretical Modelling of Unbonded Flexible Pipe Cross-Sections. Ph.D. Thesis, South Bank University, London, UK, 2000.

28. Kraincani, I.; Kebadze, E. Slip initiation and progression in helical armoring layers of unbonded flexible pipes and its effect on pipe bending behaviour. *J. Strain. Anal. Eng.* **2001**, *36*, 265–275. [CrossRef]

29. Neto, A.; Martins, C.; Pesce, C.; Meirelles, C.; Malta, E.; Neto, T.; Godinho, C. Burst prediction of flexible pipes. In Proceedings of the International Conference on Offshore Mechanics and Arctic Engineering, Shanghai, China, 6–11 June 2010; pp. 511–520.

30. Neto, A.; Martins, C.; Pesce, C.; Meirelles, C.; Malta, E.; Neto, T.; Godinho, C. Prediction of burst in flexible pipes. *J. Offshore Mech. Arct. Eng.* **2013**, *1*, 011401. [CrossRef]

31. Lanteigne, J. Theoretical estimation of the response of helically armored cables to tension, torsion, and bending. *Int. J. Appl. Mech.* **1985**, *52*, 423–432. [CrossRef]

32. Cuamatzi-Melendez, R.; Castillo-Hernández, O.; Vázquez-Hernández, A.; Albiter, A.; Vaz, M. Finite element modeling of burst failure in unbonded flexible risers. *Eng. Struct.* **2015**, *87*, 58–69. [CrossRef]

33. Ramos, J.; Kawano, A. Local structural analysis of flexible pipes subjected to traction, torsion and pressure loads. *Mar. Struct.* **2015**, *42*, 95–114. [CrossRef]

34. Ramos, R.; Pesce, C. A consistent analytical model to predict the structural behavior of flexible risers subjected to combined loads. *J. Offshore Mech. Arct. Eng.* **2004**, *126*, 141–146. [CrossRef]

35. Ramos, R.; Martins, C.; Pesce, C.; Roveri, E. Some further studies on the axial–torsional behavior of flexible risers. *J. Offshore Mech. Arct. Eng.* **2014**, *136*, 011701. [CrossRef]

36. Ren, S.; Tang, W.; Guo, J. Behavior of unbonded flexible risers subject to axial tension. *China Ocean Eng.* **2014**, *28*, 249–258. [CrossRef]

37. Ren, S.; Xue, H.; Tang, W. Analytical and numerical models to predict the behavior of unbonded flexible risers under torsion. *China Ocean Eng.* **2016**, *30*, 243–256. [CrossRef]

38. Ren, S.; Tang, W.; Kang, Z.; Geng, H. Numerical study on the axial-torsional response of an unbonded flexible riser with damaged tensile armor wires. *Appl. Ocean Res.* **2020**, *97*, 102045. [CrossRef]

39. Bahtui, A.; Bahai, H.; Alfano, G. Numerical and analytical modeling of unbonded flexible risers. *J. Offshore Mech. Arct. Eng.* **2009**, *131*, 021401. [CrossRef]

40. Zhang, M.; Chen, X.; Fu, S.; Guo, Y.; Ma, L. Theoretical and numerical analysis of bending behavior of unbonded flexible risers. *Mar. Struct.* **2015**, *44*, 311–325. [CrossRef]